





Article

Nanocrystalline Al7075 + 1 wt % Zr Alloy Prepared Using Mechanical Milling and Spark Plasma Sintering

Orsolya Molnárová ^{1,*} , Přemysl Málek ¹, Jozef Veselý ¹ , Michaela Šlapáková ¹ , Peter Minárik ¹, František Lukáč ^{2,3} , Tomáš Chráska ³, Pavel Novák ⁴ and Filip Průša ⁴

¹ Department of Physics of Materials, Faculty of Mathematics and Physics, Charles University, Ke Karlovu 5, Prague 12116, Czech Republic; malek@met.mff.cuni.cz (P.M.); vesely@gjh.sk (J.V.); slapakova@karlov.mff.cuni.cz (M.Š.); peter.minarikk@gmail.com (P.M.)

² Department of Low-Temperature Physics, Faculty of Mathematics and Physics, Charles University, V Holešovičkách 2, Prague 18000, Czech Republic; lukac@ipp.cas.cz

³ Institute of Plasma Physics of the CAS, Za Slovankou 1782/3, Prague 18200, Czech Republic; chraskat@ipp.cas.cz

⁴ Department of Metals and Corrosion Engineering, UCT Prague, Technická 5, Prague 16628, Czech Republic; Paja.Novak@vscht.cz (P.N.); Filip.Prusa@vscht.cz (F.P.)

* Correspondence: mopersze@gmail.com; Tel.: +420-2-2191-1363

Received: 24 August 2017; Accepted: 15 September 2017; Published: 20 September 2017

Abstract: The microstructure, phase composition, and microhardness of both gas-atomized and mechanically milled powders of the Al7075 + 1 wt % Zr alloy were investigated. The gas-atomized powder exhibited a cellular microstructure (grain size of a few μm) with layers of intermetallic phases along the cell boundaries. Mechanical milling (400 revolutions per minute (RPM)/8 h) resulted in a grain size reduction to the nanocrystalline range (20 to 100 nm) along with the dissolution of the intermetallic phases. Milling led to an increase in the powder's microhardness from 97 to 343 HV. Compacts prepared by spark plasma sintering (SPS) exhibited negligible porosity. The grain size of the originally gas-atomized material was retained, but the continuous layers of intermetallic phases were replaced by individual particles. Recrystallization led to a grain size increase to 365 nm in the SPS compact prepared from the originally milled powder. Small precipitates of the Al_3Zr phase were observed in the SPS compacts, and they are believed to be responsible for the retainment of the sub-microcrystalline microstructure during SPS. A more intensive precipitation in this SPS compact can be attributed to a faster diffusion due to a high density of dislocations and grain boundaries in the milled powder.

Keywords: gas atomization; mechanical milling; spark plasma sintering; microstructure; microhardness; recrystallization

1. Introduction

Materials with nanosize- or ultrafine-grained structure have received much attention in the last decades. Their yield stress is increased according to the Hall-Petch relationship. Their strength characteristics can be further improved by the introduction of a dense and homogeneous distribution of fine precipitates or dispersoids, which not only contribute to the materials' strength, but also stabilize the fine-grained microstructure. These particles can successfully pin grain boundaries and dislocations, and suppress recrystallization and grain growth.

Materials with a fine-grained structure can be, among others, prepared by a powder metallurgy (PM) route. Gas atomization based on the disintegration of a molten metal stream by high pressure

gas jets is a typical representative of rapid solidification methods which is capable of producing fine powder particles. High cooling rates (10^3 – 10^5 K/s) along with a high surface-to-volume ratio of droplets lead to a fine microstructure, extended solid solubility, and to the formation of metastable phases [1], all enhancing material strength. Further microstructural refinement can be achieved by the mechanical milling of atomized powders. Repeated flattening, fracturing, and rewelding of powder particles occurs during the milling process, and a large amount of deformation energy is introduced into the powder material. The very high strain rates lead to severe plastic deformation and high dislocation density. The self-organization of dislocations into cell networks, low-angle boundaries, and finally high-angle boundaries is considered to be the mechanism of grain refinement down to the nanoscale range [2–4]. Additionally, fine oxide and nitride particles from the powder particle surface, atmosphere, or milling agent can be introduced into the matrix during the milling process, which can further enhance strength through dispersion strengthening [5]. These dispersoids can also play an important role in maintaining powders' fine-grained structure during a subsequent consolidation process.

The microstructure and properties of PM materials can be strongly affected by the selected consolidation process. The most frequently used sintering methods, such as hot pressing (HP) or hot isostatic pressing (HIP), are based on concurrent external heating and pressing (e.g., [6,7]). The elevated temperature and prolonged heat exposure characteristic of these sintering methods can lead to recrystallization, grain growth, or massive precipitation, all decreasing the gains from atomization and milling. Spark plasma sintering (SPS) represents an alternative method that can minimize these detrimental effects. SPS combines uniaxial pressure with heating by a low-voltage direct current (DC) flowing through the sample (in the case of conductive material). A large Joule heat is evolved especially at the contact points between powder particles, and the temperature at these points can highly exceed the set one. It is claimed that SPS affects particularly the surfaces of the powder particles, and the particle cores can retain their original microstructure [8]. During SPS, the oxide layers, which are regularly present at the surfaces of powder particles, can be disrupted more efficiently than by conventional sintering techniques [7,9,10]. SPS is thus able to produce fully dense compacts at lower temperatures and in substantially shorter times than other consolidation routes, and the undesirable processes, such as recrystallization or grain growth, can be restricted.

PM processing has been successfully used in many aluminium-based materials. Both gas atomized (e.g., [11–15]) and milled (e.g., [16–19]) powders have been sintered by a variety of methods. SPS results in the lowest porosity [20], and is also very efficient in the production of a very fine-grained microstructure [19,20]. Numerous experiments have been performed on the 7xxx series of Al-based alloys. A combination of gas atomization and SPS has been used for the preparation of the Al7075 alloy with the relative density exceeding 99%. The grain size of this material was in the range of between 1 and 10 μm , and remained stable even after annealing at 500 °C [21,22]. Even finer Al7075 material with a grain size at the nano-meter scale has been prepared by a combination of milling of elemental powders followed by hot pressing [18].

Zirconium is frequently added to the Al7075 alloy for an improved stabilization of the fine-grained structure. Small precipitates of the metastable Al_3Zr phase serve as grain boundary pinners [23]. A grain size slightly exceeding 1 μm has been observed in the Al7075 + 0.7 wt % Zr [13] and 1 wt % Zr alloys [14] prepared by a combination of gas atomization and hot extrusion, and both these materials exhibited high strain rate superplasticity. Furthermore, the introduction of Al_3Zr particles displaced the border of thermal stability to higher temperatures in a cryorolled 7075 alloy in [24]. A nano-sized microstructure has been observed also in the Al7068 + 0.1 wt % Zr alloy consolidated by hot pressing [17]. Unfortunately, the relative density of this material was below 97%, which resulted in a brittle behaviour.

Whereas the commercial Al alloys are doped usually only by a few tenths wt % of Zr, the Al7075 alloy used in our research is a model material where a higher Zr content was chosen in order to emphasize the role of Zr addition in microstructural stabilization. A combination of gas atomization, mechanical milling of the powders, and spark plasma sintering was expected to result in a very

fine-grained material with minimum porosity, good microstructural stability, and good mechanical properties. A proper investigation of the microstructure and phase composition after each step of processing was performed using a variety of experimental techniques, and the findings were correlated with the microhardness.

2. Materials and Methods

The Al7075 alloy powder modified by the addition of about 1 wt % of Zr was prepared by Nanoval GmbH and Co. KG, Berlin, Germany. The alloy was atomized by nitrogen and sieved down to 50 μm . The average particle size was stated by the producer to be 20.9 μm . The atomized powder will be further denoted as Al7075Zr_A. The chemical composition of the gas-atomized powder according to X-ray fluorescence (XRF) spectroscopy is given in Table 1.

Table 1. The chemical composition of the gas atomized Al7075Zr alloy determined by XRF.

Element	wt %
Zn	6.6 ± 0.1
Mg	2.8 ± 0.1
Cu	2.2 ± 0.1
Fe	0.12 ± 0.01
Si	0.08 ± 0.01
Zr	1.30 ± 0.03
Al	Balance

High energy ball milling of the atomized powder was carried out in a Retsch PM 100 CM mill (Retsch GmbH, Haan, Germany) at room temperature. The atomized powder was dry milled in a steel tank with a speed of 400 revolutions per minute (RPM) for 8 h in an Ar atmosphere using 20 mm steel balls. The ball-to-powder ratio was 40:1. The milled powder is further denoted as Al7075Zr_M.

Both the atomized and milled powders were compacted by SPS using FCT SPS-HP25 (FCT Systeme GmbH, Effelder-Rauenstein, Germany). The scheme of the sintering process is presented in Figure 1. During consolidation, the samples were free heated up to 400 $^{\circ}\text{C}$, and the 425 $^{\circ}\text{C}$ sintering temperature was reached with a heating rate of 25 $^{\circ}\text{C}/\text{min}$. Simultaneously with temperature, the uniaxial pressure was increased up to 80 MPa. After the holding time of 4 min, the compact was free cooled and unloaded. The density of SPS compacts was measured using He pycnometry, and the sample porosity was additionally controlled by image analysis of SEM micrographs (10 images were evaluated for each material). The compacts prepared from the atomized and milled powders are further referred to as Al7075Zr_AC and Al7075Zr_MC, respectively.

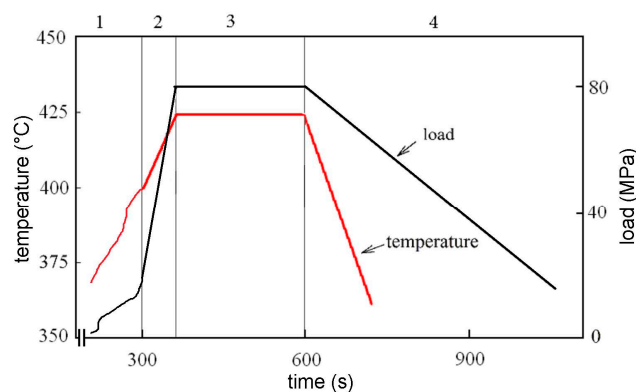


Figure 1. The scheme of the sintering process: 1: set vacuum, free heating to 400 $^{\circ}\text{C}$, applying an initial load of 20 MPa; 2: increase in temperature and load (60 s); 3: holding at a temperature of 425 $^{\circ}\text{C}$ and a load of 80 MPa (240 s); 4: free cooling and parallel unloading.

The phase composition and structural changes were investigated by X-ray diffraction (XRD) using a diffractometer D8 Discover (Bruker AXS, Brno, Czech Republic) in Bragg-Brentano geometry with a $\text{CuK}\alpha$ source and a $\text{NiK}\beta$ radiation filter. A quantitative Rietveld analysis was performed by TOPAS V5 (Bruker AXS) to determine the weight fraction of all identified phases. The sizes of coherently diffracting domains (CDD) and microstrains were evaluated from the broadening of diffraction peaks assuming that small crystallites and microstrains contribute to the broadening of the Lorentzian and Gaussian components of the pseudo-Voigt function, respectively [25].

The morphology and microstructure of the powders were investigated by light microscopy (LM) using an Olympus GX51 (Olympus, Prague, Czech Republic) microscope. The powders were cold mounted in acrylic cold mounting resin, metallographically processed, and finally etched by Dix-Keller reagent to reveal microstructure details.

Finer microstructural details were investigated by scanning electron microscopy (SEM) using an FEI Quanta 200F microscope (FEI, Brno, Czech Republic) equipped with a field emission cathode (FEG). Chemical composition was studied by energy dispersive X-ray spectroscopy (EDS) (EDAX, Nachod, Czech Republic). The grain size and grain orientation were analysed using electron backscattered diffraction (EBSD). The EBSD camera DigiView3 (EDAX, Nachod, Czech Republic) was used for signal detection, and TSL OIM 7 software (Version 7.3.0, EDAX, Nachod, Czech Republic) was used for data analysis. The preparation of samples for SEM included hot mounting (180 °C, 2.5 min) in conductive resin with carbon filler (in the case of powder samples), mechanical grinding, mechanical polishing up to 1 μm , chemical polishing with SiO_2 oxide in polishing suspension, and electro-polishing (just for EBSD).

Transmission electron microscopy (TEM) investigations were performed using a JEOL 2200FS microscope (JEOL, Peabody, USA) operated at an accelerating voltage of 200 kV. TEM specimens from powders were produced using focused ion beam (FIB) milling in a Zeiss Auriga Compact SEM microscope. The samples were extracted from a chosen powder particle embedded in conductive resin with carbon filler; further, they were milled to electron transparency and mounted onto a copper TEM grid. Interplanar spacings and angles were measured on electron diffraction patterns taken along reasonably low index axis orientations. These were then matched to crystal structures selected from inorganic crystal structure database (ICSD) [26] based on the composition criteria (EDX). Finally, the whole pattern was simulated in JEMS [27] and a match with the experimental pattern was verified.

From the SPS compacts, discs with a diameter of 3 mm were cut from a plane parallel to the direction of load applied during SPS. Thin foils for TEM observations were prepared by electrochemical thinning using a double-jet polisher, Tenupol-5, under 15 V at -15 °C in a solution of 33% nitric acid in methyl alcohol.

The strength of the materials was characterized using microhardness measurements. An automatic microhardness tester Qness Q10A+ with a Vickers indenter (Qness GmbH, Golling, Austria) was used. For the powder materials, one indent with a load of 10 N was applied to an individual particle embedded in the cold mounting resin, and the mean microhardness value was calculated from measurements performed on different powder particles. For the compact materials, indentations were performed with the applied load of 50 N on planes parallel to the direction of the applied stress during SPS. In order to obtain good statistics, areas of $4.4 \times 4.4 \text{ mm}^2$ were investigated, with a distance between individual indents of 200 μm .

3. Results

3.1. Powder Material

Gas atomization resulted in nearly spherical powder particles, as presented in Figure 2a. Excluding some very small spherical or irregular-shaped particles with a segregation-free microstructure (see the 5 times magnified detail in Figure 2a), the powder's internal microstructure is cellular. Mechanical milling significantly altered the powder's morphology: the milled powder particles have an irregular shape, and their size is several times increased in comparison with the gas-atomized

particles (Figure 2b). The internal microstructure was destroyed, and only some relatively coarse individual particles can be distinguished, which were introduced from the milling media into the material during milling.

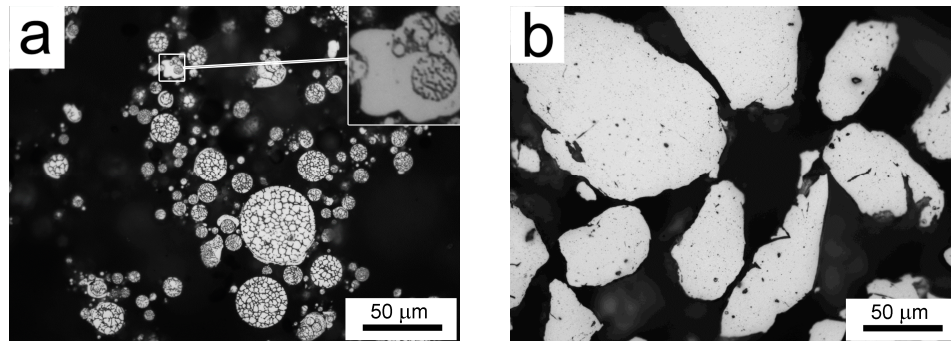


Figure 2. The morphology of (a) Al7075Zr_A and (b) Al7075Zr_M powder particles, light microscopy (LM).

A backscattered electron (BSE) micrograph of a typical representative of Al7075Zr_A powder with the corresponding EBSD map can be seen in Figure 3. The particles have a mostly cellular microstructure, with an intercellular segregation of higher atomic weight elements along the internal boundaries. However, some atomized powder particles were attached to segregation-free regions (see Figure 3a). EBSD measurements revealed that the cells can be mostly considered as grains separated by high-angle boundaries with a size close to 1 μm (Figure 3b). The SEM-EDS revealed that the boundary regions were rich in Cu, Mg, and Zn (see Figure 4).

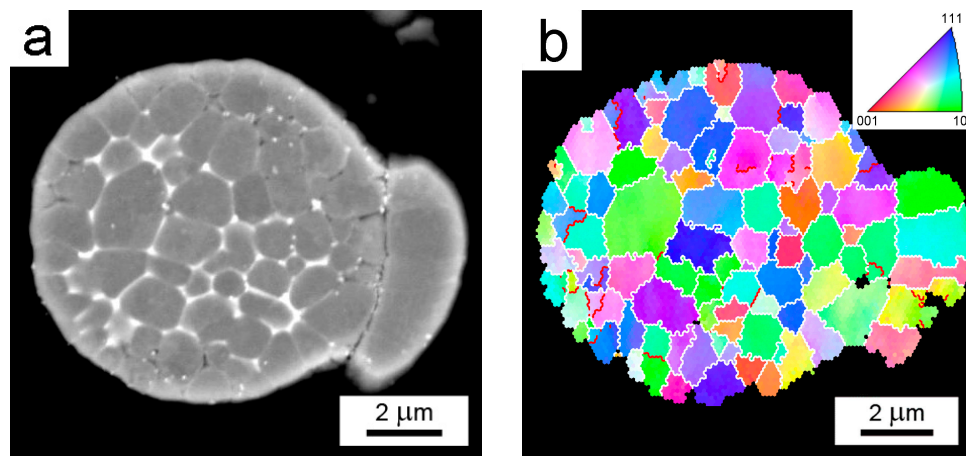


Figure 3. The solidification microstructure of the Al7075Zr_A powder particle (a) BSE contrast; (b) the corresponding electron backscattered diffraction (EBSD) micrograph and distribution of grain boundaries. Boundaries with misorientation angles above 15° in white, boundaries between 5° and 15° in red.

The BSE micrograph of the milled powder particle in Figure 5 confirms that the layers of intermetallic phases present in the Al7075Zr_A powder along the cell boundaries were completely destroyed during milling. This result was supported by the SEM-EDS analysis, which documented no segregation of the main alloying elements (Zn, Mg, and Cu). Relatively coarse bright particles visible inside the milled powder particles (see Figure 5) are contaminations integrated into the particles during the milling process. The contaminating material was present in the milling chamber as small residue from the last preceding milling process. A chemical analysis of the milled powder by XRF proved the

presence of 0.27 wt % of Ni and 0.22 wt % of Ti in the milled powder. A TEM-EDS analysis proved the presence of these elements in bright particles with a composition of around Ni₅₀Ti₅₀, but there were also particles containing only Ti. However, the volume fractions of the contaminating NiTi and Ti phases introduced during milling were too small to be detected by XRD. Due to the powder's highly deformed microstructure, no SEM-EBSD map could be obtained from the milled powder particles.

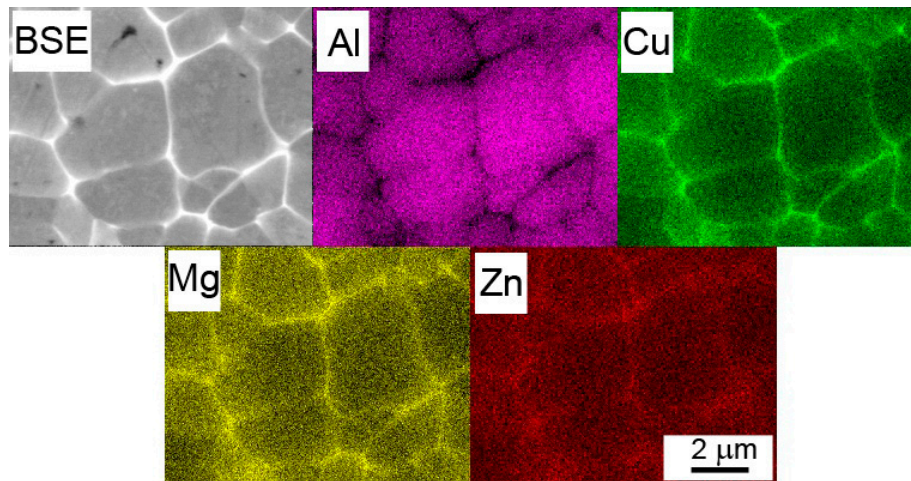


Figure 4. Element distribution in an atomized Al7075Zr_A powder particle with a cellular microstructure. BSE and the corresponding SEM-EDS maps.

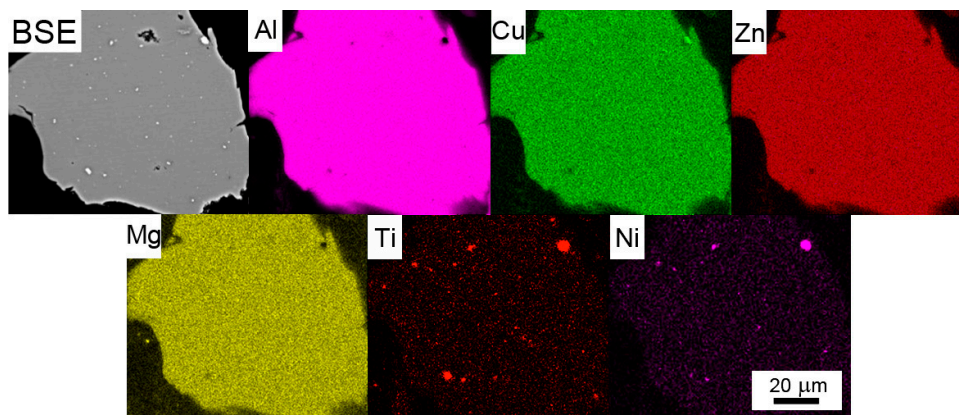


Figure 5. Element distribution in a milled Al7075Zr_M powder particle. BSE and the corresponding SEM-EDS maps.

The phase composition of both atomized and milled powders was examined using XRD. Figure 6 documents that the atomized powder contains $(Al,Zn,Cu)_{49}Mg_{32}$ phase (about 0.8 wt %), $Mg(Zn,Cu,Al)_2$ phase (the weight fraction estimated to 0.4%), and surprisingly also pure Zn (about 1.3 wt %). β marks the non fully filtered β line from the used $CuK\alpha$ source. No peaks of intermetallic phases were detected by XRD in the milled powder. The diffraction peaks of the Al matrix are in the case of the milled powder slightly shifted to higher angles. From the XRD diffraction line, the broadening in the CDD size in the milled powder was estimated to be around 64 nm. The microstrain was evaluated to be 0.0013. This analysis of XRD peaks could not be performed for the atomized powders, because the size of the CDD in the aluminium phase is above the limit of the reasonable quantification by the models used, which is estimated to be 400 nm.

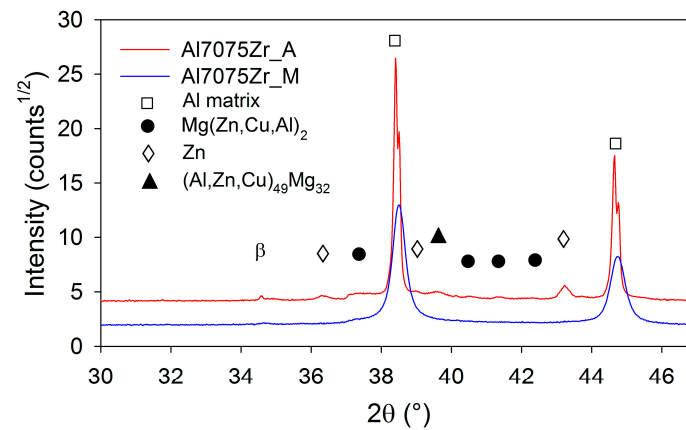


Figure 6. The comparison of XRD patterns for atomized and milled Al7075Zr powders.

A typical TEM micrograph of the atomized powder is shown in Figure 7a. The grain size is of the order of several micrometers. A mixture of intermetallic phases is present at triple points, and extends continuously along the grain boundaries (Figure 7b). Sometimes, these continuous phases are broken into a string of individual particles. These intermetallic phases were identified with the help of EDX and nanodiffraction as cubic $\text{Mg}_2\text{Cu}_5\text{Al}_6$ ($a = 0.86$ nm) and tetragonal AlCu_2 ($a = 0.60$, $c = 0.48$ nm). Moreover, orthorhombic Ga_2Mg ($a = 0.68$, $b = 1.63$, $c = 0.41$ nm) was found along with substantial Ga segregation in these boundary phases. The Ga contamination is a result of lamella preparation by FIB.

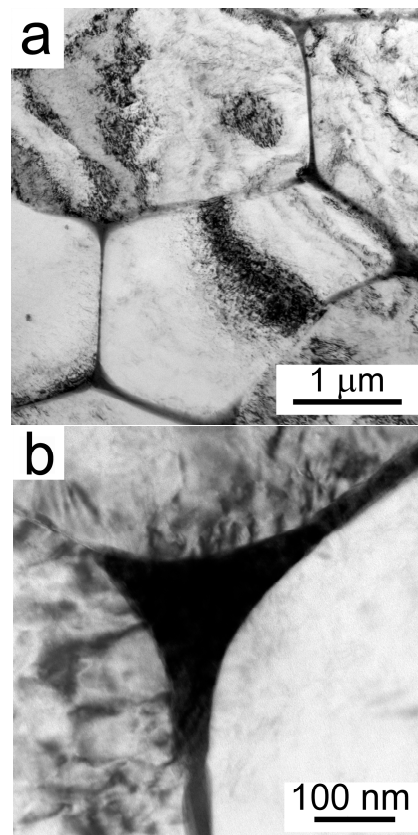


Figure 7. The microstructure of an atomized powder particle Al7075Zr_A, (a) cell interiors; (b) boundary region.

A representative bright field TEM image in Figure 8a reveals the presence of elongated grains with a size of about 20 to 100 nm in the milled powder. This size is in a good agreement with the CDD size determined from the analysis of the XRD peaks. Figure 8b displays two contaminating particles, containing Ni and Ti, embedded in the Al matrix.

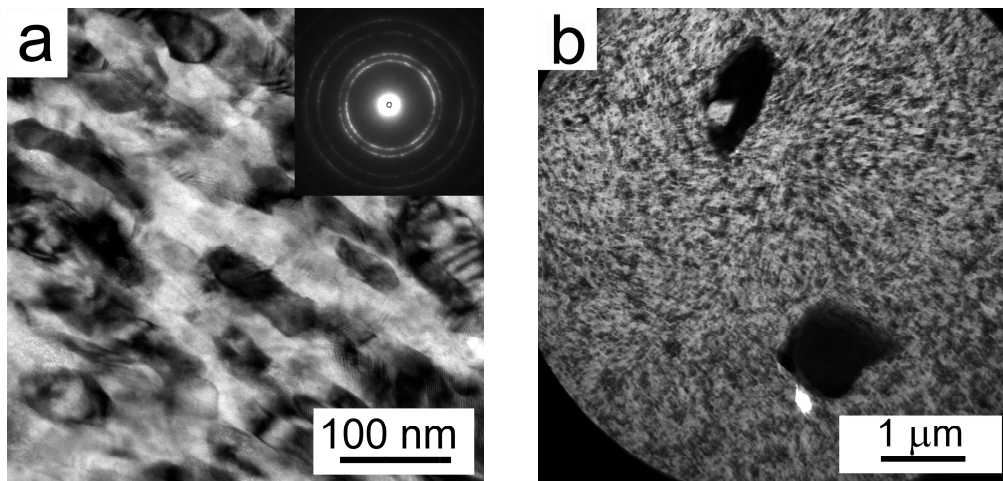


Figure 8. TEM images of the microstructure of a milled powder particle Al7075Zr_M, (a) elongated grains and (b) NiTi and Ti particles embedded in matrix.

The microhardness measurement revealed an enormous difference between the atomized and milled powders. Whereas the Al7075Zr_A powder exhibited a moderate microhardness of 97 ± 16 HV, a remarkable increase in microhardness caused by milling up to the value of 343 ± 25 HV was found in the Al7075Zr_M powder.

3.2. Compact Materials

SPS led to nearly full density compacts. The density of the Al7075Zr_AC compact was determined to be 2.80 g cm^{-3} , which is slightly below the theoretical value for the Al7075 alloy (2.81 g cm^{-3}), and the density of the Al7075Zr_MC compact was slightly higher (2.83 g cm^{-3}). The volume fraction of pores estimated by image analysis is about 0.69 vol % and 0.16 vol % for the Al7075Zr_AC and Al7075Zr_MC compacts, respectively.

Figure 9 shows the BSE micrographs of SPS compacts prepared from both atomized (a) and milled (b) powders. In the Al7075Zr_AC compact (Figure 9a), the former powder particles are still recognisable along with their mostly cellular microstructure. The boundaries of the former powder particles are decorated by coarser precipitates up to $1 \mu\text{m}$. The initially continuous layers of intercellular segregations were rearranged into semi-continuous networks of precipitates below $1 \mu\text{m}$, formed by higher atomic weight alloying elements. Furthermore, particles of a few hundred nm were found in the grain interiors. Figure 9a shows also some discontinuities at the triple points of the original powder particles. Considering the results of the porosity measurement, these discontinuities can be interpreted predominantly as pull-outs formed during the metallographic preparation of samples for SEM investigation (mechanical and electro-polishing).

The BSE micrographs of the Al7075Zr_MC compact (Figure 9b) exhibit no materials discontinuity. The large bright particles in the left bottom corner of Figure 9b are contaminating particles containing Ni and Ti. The smaller precipitates, with a size of up to $1 \mu\text{m}$, showed an increased Zn, Mg, and Cu content (Figure 10).

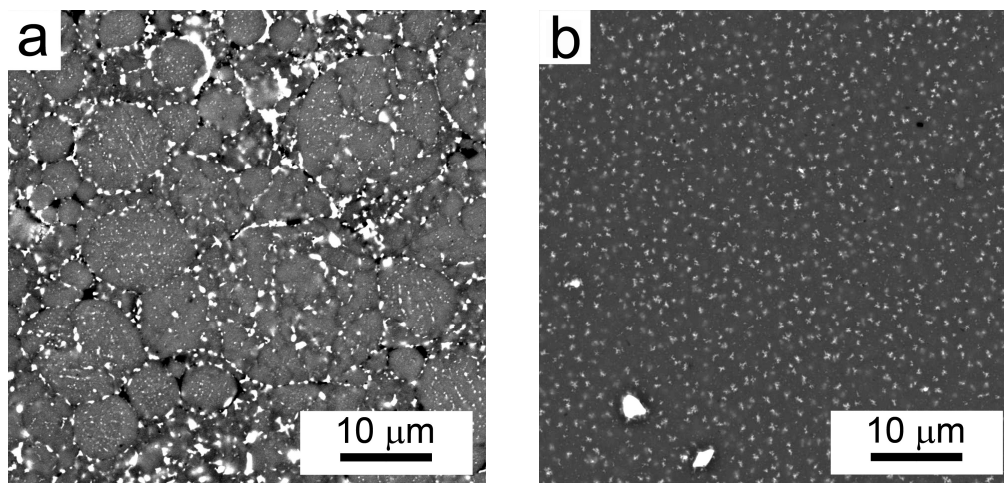


Figure 9. The microstructure of spark plasma sintering (SPS) compacts: (a) Al7075Zr_AC compact; (b) Al7075Zr_MC compact, BSE contrast.

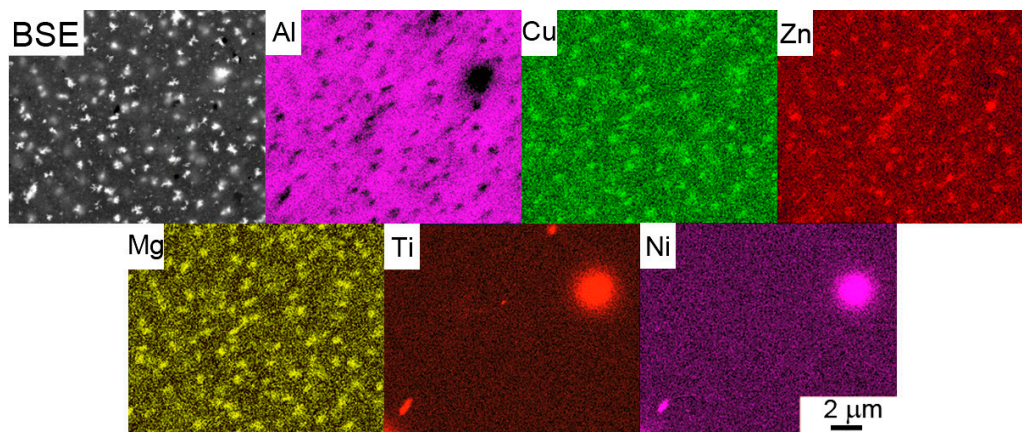


Figure 10. Element distribution in the Al7075Zr_MC compact. BSE and the corresponding SEM-EDS maps.

Quantitative information on the phase composition was obtained from the XRD measurement (Figure 11). In the Al7075Zr_AC compact, the content of $\text{Mg}(\text{Zn,Cu,Al})_2$ increased during sintering up to 1.2 wt %, the $(\text{Al,Zn,Cu})_{49}\text{Mg}_{32}$ and Zn precipitates disappeared, and a new Al_2CuMg phase was formed (1.2 wt %). In the Al7075Zr_MC compact, a $\text{Mg}(\text{Zn,Cu,Al})_2$ phase (about 3.2 wt %) and a Al_2CuMg phase (about 0.8 wt %) were formed. A very slight peak of the metastable Al_3Zr phase (corresponding to about 0.7 wt %) was also observed. The CDD size and microstrain of the Al7075Zr_MC compact (evaluated from the XRD peak broadening) was found to be (220 ± 8) nm and 0.0003, respectively. In the Al7075Zr_AC compact, the CDD size of the aluminium matrix was above the quantification limit.

An insight into the grain structure was obtained using EBSD mapping (Figure 12). The microstructure of the Al7075Zr_AC compact is represented by a mixture of smaller grains (approximately 1 μm) and coarser grains, whose size correlates with the size of the original monocrystalline gas-atomized powder particles. The mean grain size is around 3.8 μm . A completely different microstructure was observed in the Al7075Zr_MC compact; the microstructure is more homogeneous, and the mean grain size is deep in the sub-microcrystalline range at around 365 nm. The grain size distribution of both compacts is documented in Figure 13.

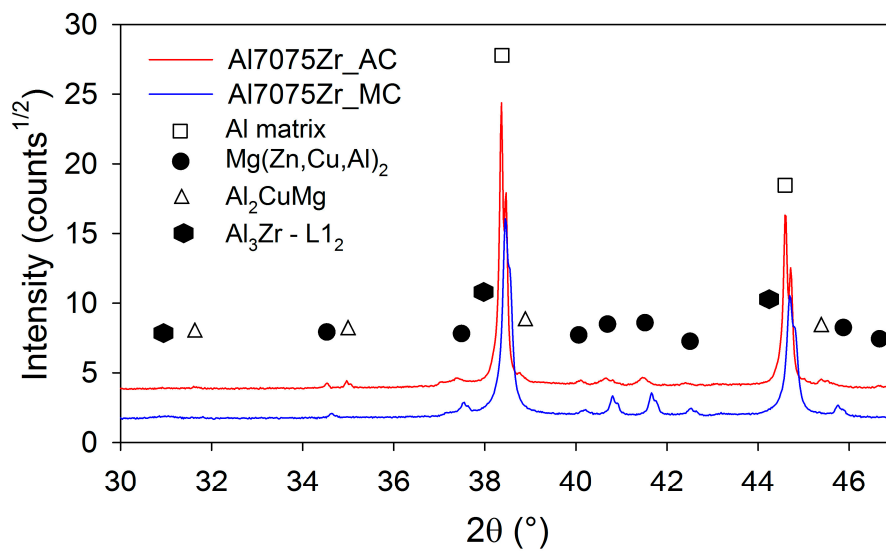


Figure 11. XRD patterns of compacts from atomized and milled 7075Zr.

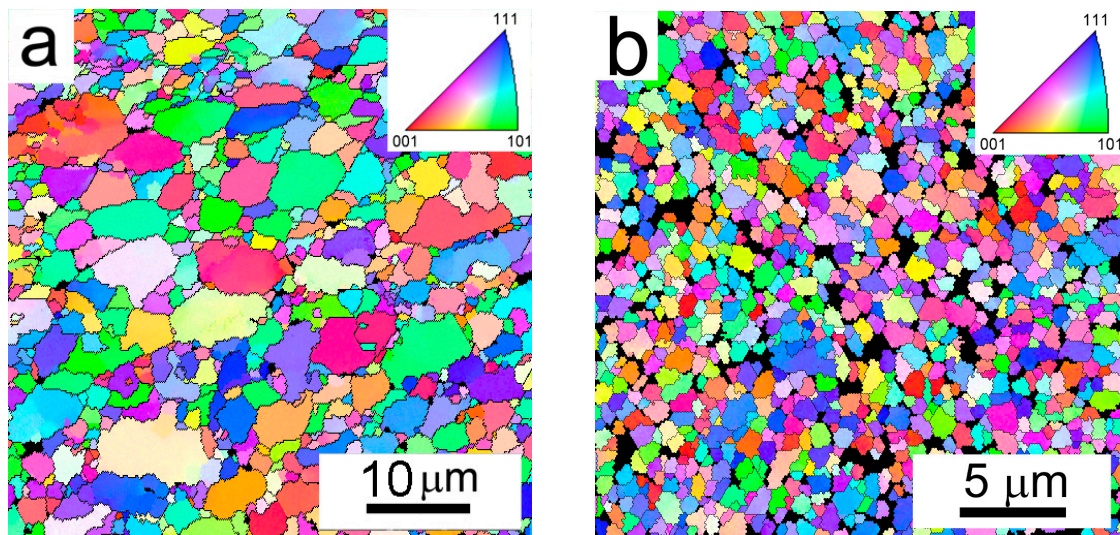


Figure 12. The microstructure of SPS compacts: (a) Al7075Zr_AC compact; and (b) Al7075Zr_MC compact, EBSD micrographs.

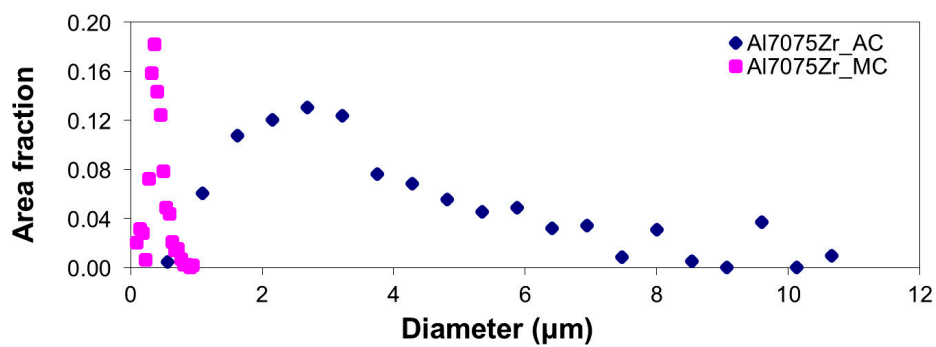


Figure 13. Grain size distribution of SPS compacts.

Along with the grain size, the misorientation of neighbouring grains can influence the material properties. Figure 14 shows the character of grain boundaries in both compacts. The images combine grain boundary map with the pattern quality image, which show the crystallographic uniformity within the interaction volume (see Figure 12). Figure 14a documents that, similarly to the atomized powder, the grains in the Al7075Zr_AC compact are separated predominantly by high-angle boundaries. The same high-angle character of grain boundaries was observed also in the Al7075Zr_MC compact (Figure 14b). The black areas observed in the Al7075Zr_MC compact, where the grain orientation could not be determined, may be caused by a too-small coherent volume or by precipitates embedded in the matrix. The corresponding distributions of misorientation angles are given in Figure 15. The fraction of high-angle boundaries was found to be above 90% in both compacts.

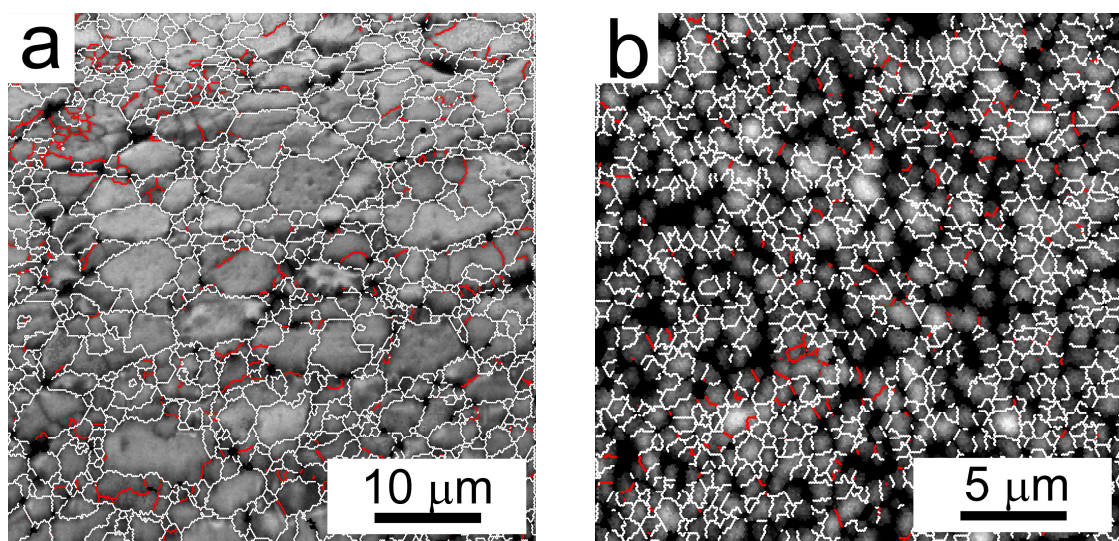


Figure 14. Distribution of grain boundaries corresponding to EBSD micrographs of Figure 12. Boundaries with misorientation angles above 15° in white and boundaries between 5° and 15° in red. (a) Al7075Zr_AC compact; (b) Al7075Zr_MC compact.

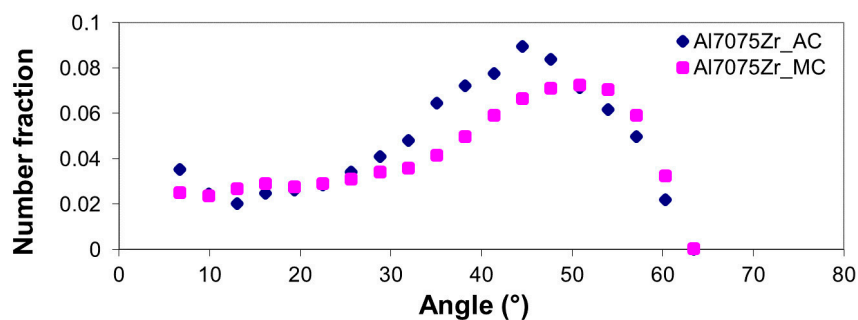


Figure 15. Distribution of grain boundary misorientation angles in both SPS compacts.

In order to examine the microstructure of the compacts in more detail, TEM investigations were performed. A semicontinuous MgO layer was found in the Al7075Zr_AC compact on the surface of the original powder particles. Further, intermetallic particles (100–500) nm were present at grain boundaries and smaller ones formed chains inside the grains (Figure 16a). A homogeneous distribution of small (a few 10 nm) particles, identified as Al₃Zr (L₁₂), was also observed, as presented in Figure 16b. Additionally, these Al₃Zr particles were aligned into a fan structure in individual grains (Figure 16c).

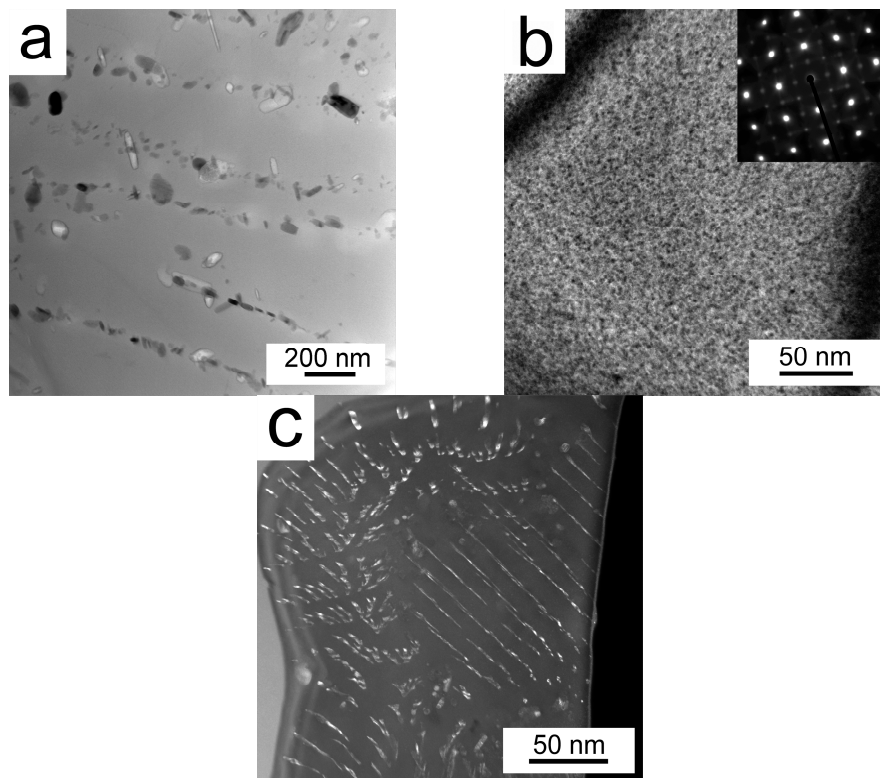


Figure 16. The microstructure of the Al7075Zr_AC compact: (a) precipitates arranged into chains; (b) homogeneous distribution of nm-sized Al₃Zr; (c) Al₃Zr particles arranged into a fan-shaped structure in dark field contrast mode, TEM.

The TEM micrograph of the Al7075Zr_MC compact (Figure 17a) shows the sub-microcrystalline microstructure of the sample. The intermetallic particles in the Al7075Zr_MC sample were found to be randomly distributed. Several particles were identified as Al₃Zr (spherical, Figure 17b) and Al₇Cu₂Fe (elongated, tetragonal $a = 0.63$ $c = 1.48$ nm). Bigger particles (~ 1 μm) were preferentially etched during the TEM sample preparation, leaving a hole in the sample. A semi-continuous MgO layer was found also between former milled powder particles by STEM-TEM. The micrograph with the corresponding EDS maps can be seen in Figure 18.

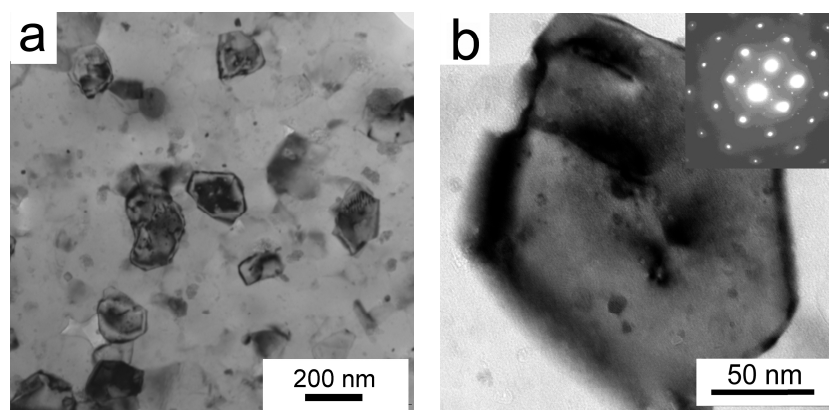


Figure 17. The microstructure of the Al7075Zr_MC compact: (a) the sub-microcrystalline microstructure of the sample; (b) a grain containing Al₃Zr particles, TEM.

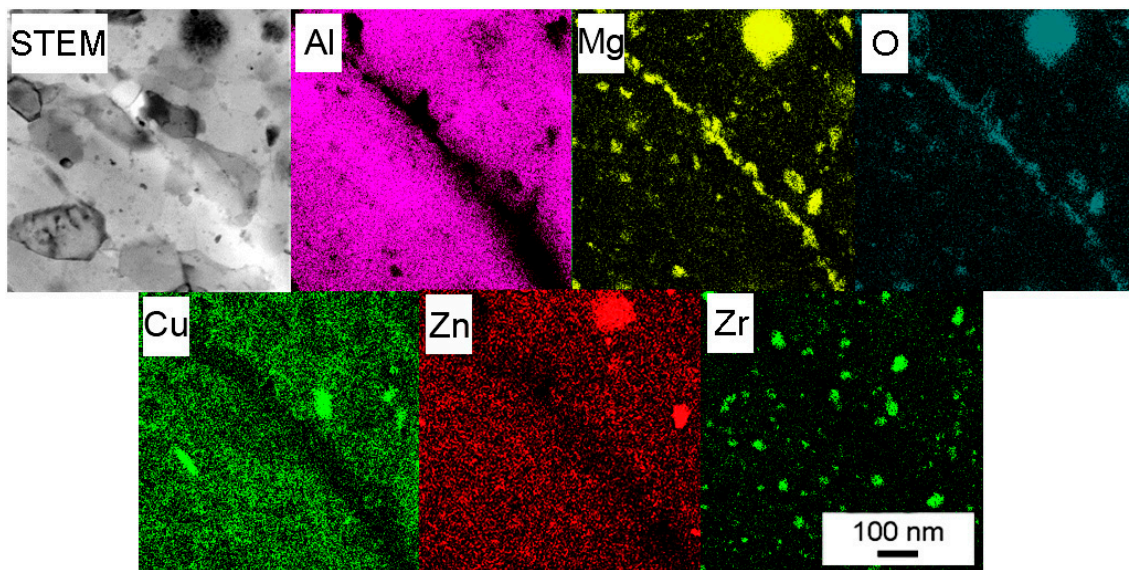


Figure 18. STEM image of the MgO layer observed in the Al7075Zr_MC compact and the corresponding EDS maps.

The microhardness measurements, because of the alloy's rapid aging, were performed 1 month after SPS, when the samples were considered to be naturally aged. The value found in the Al7075Zr_AC compact was 161 ± 6 HV. A significantly higher value of 195 ± 6 HV was measured in the Al7075Zr_MC compact.

4. Discussion

The Al7075 alloy is a commercial material, which is frequently used also for research purposes. This alloy originates its high strength especially from the precipitation sequence occurring either at room temperature or at elevated temperatures after solution treatment. An additional strength increase can be achieved by strain hardening, i.e., by the application of a large plastic deformation. Last but not least, the reduction of the grain size can contribute to a strength increase. Whereas the former treatments can be applied to materials prepared through traditional processing routes, substantial grain refinement requires a special attitude. The minimum grain size achievable by a thermomechanical treatment applied to an ingot cast material is above $10 \mu\text{m}$ [28,29]. The application of severe plastic deformation by equal channel angular pressing (ECAP) made it possible to reduce the grain size down to approximately $1 \mu\text{m}$; however, the fraction of high-angle boundaries is usually only slightly above 50%, so that many of these "grains" should be more correctly described as subgrains [30]. Powder metallurgy represents an alternative route in the processing of very fine-grained materials. Both rapid solidification methods and the mechanical milling of powders were used in our research.

Gas atomization is a typical representative of a rapid solidification technique. A high temperature gradient in the liquid phase and a high rate of solidification front movement are typical for the onset of solidification, and can result in a featureless (segregation-free) microstructure in very small droplets. In our material, such a segregation-free microstructure was also found in satellites attached to some coarser droplets (see insert in Figures 2a and 3a). The connection of smaller solid powder particles onto larger melt droplets can be attributed to a turbulent flow of particles and gas during atomization. A gradual decrease in the temperature gradient and in the rate of the solidification front results in a breakdown of planar solidification front and a formation of cellular, columnar, or dendritic microstructures [31,32]. A mixture of dendritic and cellular microstructure has been observed in the gas-atomized Al7075 alloy, with a mean droplet size of about $50 \mu\text{m}$ [21,22,33,34]. Due to the smaller mean droplet size of our material (about $20 \mu\text{m}$), the cellular microstructure is the prevailing

microstructure type. The cell size in the droplets is in the order of μm (Figure 3b), which is comparable to the grain size of the materials prepared using ECAP from ingot cast material. Nevertheless, most of the cells are separated by high-angle grain boundaries.

The powder's microstructure was completely changed by mechanical milling. The milling process consists of the flattening, fracturing, and rewelding of powder particles, which leads to alterations in powder particles' morphology, size, and microstructure. The former spherical powder particles with a size below $20\ \mu\text{m}$ became irregular-shaped, and their size increased to up to $200\ \mu\text{m}$ during the milling process. Contrary to the gas-atomized powder, it was not possible to obtain diffraction patterns from the milled powder during EBSD measurements. The explanation can be found in a too-small size of the coherently diffracting volume. According to [35], the minimum spatial resolution for aluminium is approximately $60\ \text{nm}$ using tungsten-filament SEM and 20 to $30\ \text{nm}$ using FEG-SEM. Both the evaluation of the crystallite size from the broadening of XRD peaks and the TEM investigation of the milled powder particles confirmed a nanocrystalline microstructure with the grain size between 20 and $100\ \text{nm}$ (Figure 8), which is comparable with the spatial resolution limit for EBSD. A similar grain size was observed in an AlZnMgCuZr alloy after mechanical milling for $40\ \text{h}$ from elemental powders ($27\ \text{nm}$) [17] in an Al7075 alloy after cryomilling for $10\ \text{h}$ ($28\ \text{nm}$) [36] and in the same alloy milled at room temperature for $20\ \text{h}$ ($26\ \text{nm}$) [18]. A comparison with our results shows that the rate of grain refinement is significantly higher in our case.

Spark plasma sintering was used for the consolidation of powders. The nature of SPS is not fully understood, but a range of models can be found in the literature [37]. It is believed that, beside the applied pressure, local electric and magnetic fields can activate the powder's surface, help to break up and remove oxide layers present on the surface of powder particles handled without an inert atmosphere, and promote full densification. Our results confirmed (in accordance with previous experiments on other Al-based alloys [20,21,38,39]) that SPS is very efficient in the preparation of compacts with nearly full density. The slightly lower density of the Al7075Zr_AC compact (as compared to the theoretical value) may be caused by the presence of some retained oxide particles rather than by porosity. The slightly higher density of the Al7075Zr_MC compact reflects probably the contamination by Ni and Ti during milling. Nearly negligible porosity was verified also by an image analysis of the SEM micrographs.

As already mentioned in the introduction, the temperature gradient along the powder particle radius causes necks to be formed between adjacent powder particles leading to material densification, whereas the powder particle interiors are not significantly influenced and retain their original microstructure. This has been observed in many materials, including a gas-atomized Al7075 alloy [21,34]. The present experiments revealed that no massive grain growth occurred during SPS of the gas-atomized powder (Figure 12a). The smaller grains observed in the Al7075Zr_AC compact correspond to cells present in the original coarser gas-atomized droplets; the size of the coarser grains in the Al7075Zr_AC compact corresponds to the size of the original smaller droplets present in the atomized material. It can be expected that these small droplets had originally a featureless microstructure due to a higher rate of solidification. Although two types of interfaces are present in the compact (original cell boundaries and boundaries between original droplets), both of them predominantly have a high-angle character (Figure 14).

Mechanical milling introduces a severe plastic deformation into powder particles. The stored deformation energy represents a strong driving force for recrystallization, which can be expected to occur during SPS at $425\ ^\circ\text{C}$ (despite a very short exposition to elevated temperatures). All experimental methods used in our research proved that there were significant microstructure changes in the Al7075Zr_MC compact. TEM revealed that the microstructure consisted of recrystallized equiaxed grains with a size on the order of $100\ \text{nm}$. XRD documented an increase in the crystallite size and a decrease in strain in comparison with the milled powder. Finally, the EBSD experiments showed a very homogeneous sub-microcrystalline microstructure. Grains with a mean size of below $400\ \text{nm}$ are separated predominantly by high-angle grain boundaries. This structure is significantly finer and

more homogeneous than that observed in the Al7075Zr_AC compact (Figure 12a) or in the ECAP material [30].

The mechanical properties of the Al7075-based alloys are strongly influenced by their phase composition, which is rather complicated. It has been found in ingot metallurgical material that the main alloying elements Zn and Mg are engaged in the following precipitation sequence: supersaturated solid solution-Guinier-Preston zones-metastable η' phase-stable η -MgZn₂ phase [40–42]. The solution treatment is applied at temperatures above 470 °C, which is slightly above the SPS sintering temperature used in our experiment. The maximum strength is observed in the material containing Guinier-Preston zones and metastable η' particles. Such phase composition can be formed either during annealing at temperatures close to 140 °C or during a long-term stay at room temperature, which was the case for our materials. However, this precipitation sequence can be modified by chemical composition, the presence of microstructure defects, or further sites for heterogeneous nucleation (e.g., primary particles rich in Fe or Si), and therefore also other complex phases containing e.g., Cu can be formed. Additionally, our material is doped with Zr, which should form Al₃Zr particles stabilizing the fine-grained microstructure [23,43,44]. It can be expected that precipitation sequences are strongly influenced by non-traditional processing routes, such as rapid solidification, milling, or sintering at elevated temperatures. Therefore, the phase composition after different processing steps was investigated.

The EDS experiments performed on the gas-atomized powder revealed the presence of Zn, Mg, and Cu in the cell boundaries of most powder particles. The peaks of phases of the type Mg(Zn,Cu,Al)₂ and (Al,Zn,Cu)₄₉Mg₃₂ were observed in XRD. Both phases probably also contain Cu; however, this hypothesis cannot be proved by XRD because of the very low weight fraction of both these phases (below 1%). Similar results have been found in the gas-atomized Al7075 alloy with a coarser droplet size [21,22]. No peaks of the Al₃Zr phase were observed despite a nearly negligible equilibrium solubility limit of Zr in Al [45]. It can be supposed that the Zr was nearly completely dissolved in the Al-based matrix due to rapid solidification. A similar result has been found in a melt-spun AlZnMgCuZr alloy [46].

The XRD experiment revealed no peaks of any intermetallic phases in the as-milled powder. The precipitates present in the gas-atomized powder were dissolved or their fraction decreased to under the limit of detectability of the used method. Simultaneously, as a result of the dissolution of the alloying elements in the Al-matrix, the Al peak was slightly shifted. The dissolution of the alloying elements altered the lattice parameters of the matrix. In accordance with the element's atomic radius, Zn and Cu shifted the peak toward higher angles (causing a lattice shrinkage) and Mg toward lower angles (expanding the lattice). TEM investigations confirmed the precipitate-free microstructure of the milled powder. A similar process of precipitate dissolution during milling has been observed in mechanically alloyed Al7075 after 15 h of milling [47], in a mechanically alloyed Al-Zn-Mg-Cu-Zr alloy after 40 h of milling [17], in a spray-atomized 7075 alloy after 10 h of cryomilling [36], and in a mechanically milled 7075 alloy after 20 h of milling [18]. This extension of solubility can be attributed to enhanced diffusivity due to an increased dislocation density and volume fraction of atoms in the grain boundary area [5,48].

The temperature of SPS (425 °C) is high enough to partially dissolve the phases Mg(Zn,Cu,Al)₂ and (Al,Zn,Cu)₄₉Mg₃₂ present in the cell boundaries of gas-atomized droplets [49,50]. New precipitates are then formed during slow cooling from the SPS temperature. Due to a short thermal exposure during SPS, the solute atoms could not diffuse over a long distance and new precipitates are formed, especially at places where continuous layers of intermetallic phases were located in gas-atomized droplets, i.e., in cell boundaries. New precipitates are formed also at new boundaries formed during SPS between original droplets. The weight fraction of precipitates is higher in the SPS compact than in the gas-atomized droplets. This result is not surprising if the metastable state of the gas-atomized material is considered. On the other side, the temperature and especially the duration of SPS are not high enough for a remarkable precipitation of the Al₃Zr phase in the Al7075Zr_AC compact because

of a very slow diffusion of Zr in the Al matrix [51]. This is in agreement with experiments performed in the melt-spun AlZnMgCuZr alloy, which proved the formation of the $L1_2$ Al_3Zr phase during annealing for 1 h at a temperature as high as 460 °C [46]. The presence of Al_3Zr particles was observed only by TEM investigations. Some grains contained homogeneously distributed Al_3Zr particles, while in other grains a fan-shaped arrangement was observed. This inhomogeneous distribution in individual grains is in correspondence with the literature.

Although the scheme of SPS was the same in both the atomized and milled powders, the resulting phase composition, and especially the distribution of precipitates, is different in both SPS compacts. The weight fraction of the main strengthening phase $Mg(Zn,Cu,Al)_2$ is significantly higher in the Al7075Zr_MC compact. Similarly, only the Al7075Zr_MC compact contains the Al_3Zr phase in a volume fraction sufficient for detection by XRD. It can be supposed that the high density of dislocations and grain boundaries in the milled powder enhanced the diffusion processes in comparison with the atomized material so that the precipitation processes were accelerated. Intensive milling results not only in the dissolution of precipitates present in the gas-atomized droplets but also in a more homogeneous distribution of solutes. As a consequence, the precipitates formed during SPS are more homogeneously distributed. Further, the presence of Mg oxide, especially along the boundaries of the original powder particles, was also detected. It was shown in [9,52] that even a small amount of Mg deoxidizes the amorphous surface layer of the Al oxide and forms new Mg-containing crystalline particles. The fine MgO particles can be also introduced into the powder particle interior during milling.

The microhardness of an atomized powder is determined predominantly by its phase composition. The 7xxx series Al alloys are known to exhibit natural aging at room temperature if prepared in a supersaturated state. The diffusion rate of the main alloying elements (Zn and Mg) is sufficiently high already at room temperature and redistribution of these solute atoms can occur. The atomized powder was stored after its preparation for a long time at room temperature, and it can be supposed that its phase composition is stable. The observed microhardness value of 97 ± 16 HV is deeply below the value achieved in the peak-aged ingot metallurgical Al7075 alloy (170 HV) [40], and reflects the presence of coarse layers of intermetallic phases along the cell boundaries in the gas-atomized powder droplets. The same microhardness values have been found in the gas-atomized 7075 + 1 wt % Zr powder with a larger droplet size (98 ± 18 HV) [33] and in the gas-atomized Al7075 powder (95 ± 18 HV) [21]. This comparison shows negligible hardening effects of droplet size and Zr addition within the scatter of measured microhardness values. A similar low effect of Zr addition to the AlZnMgCu alloy was reported in [32], where the microhardness of melt-spun ribbons was measured.

The milling of atomized powder particles introduced a large deformation energy into the material, and results in a grain refinement to the nanometer scale. Consequently, an extremely high microhardness value of 343 ± 25 HV was found. Although no optimization of the phase composition was performed, this value is about twofold of that observed in the peak-aged ingot metallurgical Al7075 alloy [40] or in the melt-spun ribbons of the AlZnMgCu + 1 wt % Zr alloy after optimized thermal treatment (186 HV) [46]. Figure 5 shows that the milled powder particles are contaminated by particles containing Ti and Ni. However, these particles are relatively coarse, and it is improbable that they could be responsible for the high microhardness. Additionally, as yet unpublished results obtained on the Al7075 alloy milled at the same conditions show a slightly lower microhardness despite a larger volume fraction of these contaminating particles present in this alloy. On the other side, the oxide particles introduced into the powder particles' interiors during milling could strengthen the material [5,10]. Surprisingly, the microhardness found in our milled material is significantly higher than that measured in the Al7075 alloy milled at cryotemperatures (220 ± 20 HV) using another milling device [34]. This comparison suggests that the type of milling device has an important influence because of the different amounts of introduced deformation. The high efficiency of the mill used in our experiment can also explain the shorter times necessary for the complete dissolution of intermetallic phases in comparison with the literature [17,18].

SPS influences significantly the strength of the materials. An increase in microhardness from 97 ± 16 HV up to 161 ± 6 HV was observed in the Al7075Zr_AC compact, while a decrease from 343 ± 25 HV to 195 ± 6 HV was found in the Al7075Zr_MC compact. These changes can be explained by an alteration in the microstructure and phase composition described above. In the Al7075Zr_AC compact, a partial dissolution occurring during sintering is followed by the formation of new precipitates during slow cooling from sintering temperature and during a long-term stay at room temperature between the sintering and microhardness measurement. Especially, the small $\text{Mg}(\text{Zn,Cu,Al})_2$ precipitates (Figure 16a) are believed to produce the main hardening effect. In the Al7075Zr_MC compact, similar precipitation processes occur. On the other side, a recrystallization of the severely deformed microstructure of the milled powder occurred during SPS and resulted in a decrease in dislocation density and an increase in grain size (compare Figures 8a and 17a); both of these processes reduce the material strength. Nevertheless, the microhardness is still close to the value of 200 HV, which is about 20% higher than that of the peak-aged ingot metallurgical counterpart. Especially, the sub-microcrystalline microstructure is believed to be responsible for this high microhardness.

5. Conclusions

1. The Al7075Zr compacts with very low porosity (below 1 vol %) were prepared from gas-atomized and milled powders by spark plasma sintering.
2. The gas-atomized powder has predominantly a cellular microstructure. Cells of a size typically close to 1 μm are separated by high-angle boundaries decorated by continuous layers of intermetallic phases.
3. The milled powder has a nanocrystalline microstructure, with a grain size of between 20 and 100 nm. The very small grain size simultaneously with a large strain introduced during milling results in a broadening of XRD peaks. Milling also leads to a dissolution of intermetallic phases present in the original gas-atomized powder.
4. SPS does not significantly change the microstructure of the atomized powder: the grain size corresponds to the size of the cells or to the size of smaller atomized droplets with an originally segregation-free microstructure and are separated by high-angle boundaries. The continuous layers of intermetallic phases located along the cell boundaries of atomized droplets are replaced by discrete precipitates formed predominantly at the same places. Some finer precipitates of the $\text{Mg}(\text{Zn,Cu,Al})_2$ and Al_2CuMg phases are formed in the grain's interior. No peaks from the Al_3Zr phase were found.
5. Recrystallization occurs during the SPS of milled powders. A reduction in introduced strain and an increase in the mean grain size of up to 365 nm was observed. The grains are separated predominantly by high-angle boundaries. A faster precipitation of the $\text{Mg}(\text{Zn,Cu,Al})_2$ and Al_3Zr phases can be explained by an accelerated diffusion caused by a high density of dislocations and grain boundaries in the milled powder.
6. An extremely high microhardness value (343 HV) was observed in the milled powder. A high density of dislocation and very small (nanocrystalline) grain size are predominantly responsible for this value.
7. SPS increases the microhardness of the originally atomized material from 97 to 161 HV. This increase results from the formation of small precipitates during slow cooling from the temperature of sintering and during a long-term stay at room temperature (natural aging).
8. The microhardness of the originally milled material is reduced from 343 to 195 HV during SPS. This reduction can be explained by recrystallization, a decrease in dislocation density, and an increase in the grain size. Despite this, the microhardness is about 20% higher than that of the peak-aged ingot metallurgical counterpart.
9. The contribution of Zr addition to the material strength is relatively small. The Al_3Zr is believed to significantly contribute to the retaining of a fine microstructure during the SPS process.

Acknowledgments: This work was financially supported by the grant GACR 15-15609S. One author, Orsolya Molnárová, is grateful for financial support from the project “Nanomaterialscentre for advanced applications”, Project No. CZ.02.1.01/0.0/0.0/15_003/0000485 financed by ERDF and the grant SVV-2017-260213. The authors are grateful to Hanka Becker (TU Bergakademie Freiberg, Germany) for spark plasma sintering.

Author Contributions: Přemysl Málek, Tomáš Chráska, and Pavel Novák conceived and designed the experiments; Tomáš Chráska carried out the density measurement; František Lukáč accomplished the XRD measurements and analyzed the data; Michaela Šlapáková completed the EBSD measurement, Peter Minárik prepared the TEM samples from powder material and conducted EBSD measurement, Filip Průša milled the powder, Orsolya Molnárová performed the LM, SEM, EDS, and microhardness measurements and analyzed the data, Jozef Veselý carried out TEM investigation, and Přemysl Málek and Orsolya Molnárová wrote the paper.

Conflicts of Interest: The authors declare no conflict of interest.

References

1. Lawley, A. Trends in Atomization and Consolidation of Powders for High-Temperature Aerospace Materials. In *MiCon 86: Optimization of Processing, Properties, and Service Performance Through Microstructural Control*; ASTM STP 979; Bramfitt, B.L., Benn, R.C., Brinkmann, C.R., Voort, G.F.V., Eds.; American Society for Testing and Materials: Philadelphia, PA, USA, 1988; pp. 193–201. [[CrossRef](#)]
2. Bachaga, T.; Daly, R.; Escoda, L.; Suñol, J.J.; Khitouni, M. Amorphization of Al₅₀(Fe₂B)₃₀Nb₂₀ mixture by mechanical alloying. *J. Metall. Mater. Trans. A* **2013**, *44*, 4718–4724. [[CrossRef](#)]
3. Makhlof, M.B.; Bachaga, T.; Suñol, J.J.; Dammak, M.; Khitouni, M. Synthesis and Characterization of Nanocrystalline Al-20 at. % Cu Powders Produced by Mechanical Alloying. *Metals* **2016**, *6*, 145. [[CrossRef](#)]
4. Fecht, H.-J. Nanostructure formation by mechanical attrition. *Nanostruct. Mater.* **1995**, *6*, 33–42. [[CrossRef](#)]
5. Suryanarayana, C. Mechanical alloying and milling. *Prog. Mater. Sci.* **2001**, *46*, 1–184. [[CrossRef](#)]
6. Orru, R.; Licheri, R.; Locci, A.M.; Cincotti, A.; Cao, G. Consolidation/synthesis of materials by electric current activated/assisted sintering. *Mater. Sci. Eng. R* **2009**, *63*, 127–287. [[CrossRef](#)]
7. Guillon, O.; Gonzalez-Julian, J.; Dargatz, B.; Kessel, T.; Schiering, G.; Räthel, J.; Herrmann, M. Field-Assisted Sintering Technology/Spark Plasma Sintering: Mechanisms, Materials, and Technology Developments. *Adv. Eng. Mater.* **2014**, *16*, 830–849. [[CrossRef](#)]
8. Suarez, M.; Fernandez, A.; Menendez, J.L.; Torrecillas, R.; Kessel, H.U.; Hennicke, J.; Kirchner, R.; Kessel, T. Challenges and Opportunities for Spark Plasma Sintering: A Key Technology for a New Generation of Materials. In *Sintering Applications*; Ertug, B., Ed.; InTech: Rijeka, Croatia, 2013; pp. 319–342. [[CrossRef](#)]
9. Kwon, H.; Park, D.H.; Park, Y.; Silvain, J.F.; Kawasaki, A.; Park, Y. Spark plasma sintering behavior of pure aluminium depending on various sintering temperatures. *Met. Mater. Int.* **2010**, *16*, 71–75. [[CrossRef](#)]
10. Salem, H.G.; Sadek, A.A. Fabrication of High Performance PM Nanocrystalline Bulk AA2124. *J. Mater. Eng. Perform.* **2010**, *19*, 356–367. [[CrossRef](#)]
11. Rajabi, M.; Vahidi, M.; Simchi, A.; Davami, P. Effect of rapid solidification on the microstructure and mechanical properties of hot-pressed Al-20Si-5Fe alloys. *Mater. Charact.* **2009**, *60*, 1370–1381. [[CrossRef](#)]
12. Malek, P.; Janecek, M.; Bartuska, P. Structure and properties of a powder metallurgy Al-Zr-Ti alloy. *Kovove Mater.* **2002**, *40*, 371–388. Available online: https://www.researchgate.net/publication/287630953_Structure_and_properties_of_a_powder_metallurgy_Al-Zr-Ti_alloy (accessed on 4 April 2017).
13. Matsuki, K.; Iwaki, M.; Tokiyawa, M.; Murakami, Z. Microstructural evolution during initial stage of high-strain rate superplastic deformation in powder metallurgical 7475 Al-0.7Zr alloy. *Mater. Sci. Technol.* **1991**, *7*, 513–519. [[CrossRef](#)]
14. Malek, P.; Erlebach, J.; Cieslar, M.; Knoop, F.M. Superplasticity in an Al-Zn-Mg-Cu-Zr alloy prepared by powder metallurgy. *Phys. Status Solidi A* **1996**, *157*, 275–286. [[CrossRef](#)]
15. Rokni, M.R.; Widener, C.A.; Crawford, G.A. Microstructural evolution of 7075 Al gas atomized powder and high-pressure cold sprayed deposition. *Surf. Coat. Technol.* **2014**, *251*, 254–263. [[CrossRef](#)]
16. Asgharzadeh, H.; Simchi, A.; Kim, H.S. Microstructural features, texture and strengthening mechanisms of nanostructured AA6063 alloy processed by powder metallurgy. *Mater. Sci. Eng. A* **2011**, *528*, 3981–3989. [[CrossRef](#)]
17. Azimi, A.; Shokuhfar, A.; Zolriasatein, A. Nanostructured Al-Zn-Mg-Cu-Zr alloy prepared by mechanical alloying followed by hot pressing. *Mater. Sci. Eng. A* **2014**, *595*, 124–130. [[CrossRef](#)]

18. Das, T.; Karunanithi, R.; Sinha, A.; Ghosh, K.S.; Bera, S. Deformation, decomposition and hardening of nano Al7075 alloy prepared by mechanical milling and hot pressing. *Adv. Powder Technol.* **2016**, *27*, 1874–1877. [[CrossRef](#)]
19. Saheb, N.; Aliyu, I.K.; Hassan, S.F.; Al-Aqeeli, N. Matrix structure evolution and nanoreinforcement distribution in mechanically milled and spark plasma sintered Al-SiC nanocomposites. *Materials* **2014**, *7*, 6748–6767. [[CrossRef](#)] [[PubMed](#)]
20. Al-Aqeeli, N. Processing of CNTs reinforced Al-based nanocomposites using different consolidation techniques. *J. Nanomater.* **2013**, 1–10. [[CrossRef](#)]
21. Molnárová, O.; Málek, P.; Lukáč, F.; Chráska, T. Spark Plasma Sintering of a Gas Atomized Al7075 Alloy: Microstructure and Properties. *Materials* **2016**, *9*, 1004. [[CrossRef](#)] [[PubMed](#)]
22. Becker, H.; Dopita, M.; Stráská, J.; Málek, P.; Vilémová, M.; Rafaja, D. Microstructure and properties of spark plasma sintered Al-Zn-Mg-Cu alloy. *Acta Phys. Pol. A* **2015**, *128*, 602–605. [[CrossRef](#)]
23. Zhang, J.C.; Ding, D.Y.; Zhang, W.L.; Kang, S.H.; Xu, X.L.; Gao, Y.J.; Chen, G.Z.; Chen, W.G.; You, X.H. Effect of Zr addition on microstructure and properties of Al-Mn-Si-Zn-based alloy. *Trans. Nonferrous Met. Soc. China* **2014**, *24*, 3872–3878. [[CrossRef](#)]
24. Panigrahi, S.K.; Jayaganthan, R. Effect of Annealing on Thermal Stability, Precipitate Evolution, and Mechanical Properties of Cryorolled Al 7075 Alloy. *Met. Mater. Trans. A* **2011**, *42*, 3208–3217. [[CrossRef](#)]
25. Tagliente, M.A.; Massaro, M. Strain-driven (0 0 2) preferred orientation of ZnO nanoparticles in ion-implanted silica. *Nucl. Instrum. Methods Phys. Res. B* **2008**, *266*, 1055–1061. [[CrossRef](#)]
26. Hellebrandt, M. The Inorganic Crystal Structure Database (ICSD)—Present and Future. *Crystallogr. Rev.* **2004**, *10*, 17–22. [[CrossRef](#)]
27. Stadelmann, P.A. EMS—A software package for electron diffraction analysis and HREM image simulation in materials science. *Ultramicroscopy* **1987**, *21*, 131–145. [[CrossRef](#)]
28. Wert, J.A.; Paton, N.E.; Hamilton, C.H.; Mahoney, M. Grain-refinement in 7075 Aluminum by thermomechanical processing. *Met. Trans. A* **1981**, *12*, 1267–1276. [[CrossRef](#)]
29. Malek, P. Superplasticity in an Al-Zn-Mg-Cu alloy. *Mater. Sci. Eng. A* **1991**, *137*, 21–26. [[CrossRef](#)]
30. Turba, K.; Malek, P.; Rauch, E.F.; Cieslar, M. High strain rate superplasticity in a Zr and Sc modified 7075 aluminum alloy produced by ECAP. *Mater. Sci. Forum* **2008**, *584–586*, 164–169. [[CrossRef](#)]
31. Devaraj, S.; Sankaran, S.; Kumar, R. Influence of spark plasma sintering temperature on the densification, microstructure and mechanical properties of Al-4.5 wt %Cu alloy. *Acta Metall. Sin.* **2013**, *26*, 761–771. [[CrossRef](#)]
32. Gupta, M.; Mohamed, F.A.; Lavernia, E.J. Solidification characteristics of atomized Al-Ti powders. *Scr. Metall. Mater.* **1992**, *26*, 697–702. [[CrossRef](#)]
33. Molnárová, O.; Málek, P.; Becker, H. The investigation of the Al7075+ 1 wt % Zr alloy prepared using spark plasma sintering. In Proceedings of the METAL 2015: 24th International Conference on Metallurgy and Materials, Brno, Czech Republic, 3–5 June 2015; pp. 1221–1226.
34. Molnarova, O.; Malek, P.; Németh, G.; Kozlík, J.; Lukáč, F.; Chráska, T.; Cinert, J. The investigation of an Al7075 alloy prepared by spark plasma sintering of milled powders. In Proceedings of the METAL 2016: 25th Anniversary International Conference on Metallurgy and Materials, Brno, Czech Republic, 25–27 May 2016; pp. 1200–1205.
35. Humphreys, F.J.; Huang, Y.; Brough, I.I.; Harris, C. Electron backscatter diffraction of grain and subgrain structures-resolution considerations. *J. Microsc.* **1999**, *195*, 212–216. [[CrossRef](#)] [[PubMed](#)]
36. Chen, H.B.; Tao, K.; Yang, B.; Zhang, J.S. Nanostructured Al-Zn-Mg-Cu alloy synthesized by cryomilling and spark plasma sintering. *Trans. Nonferrous Met. Soc. China* **2009**, *19*, 1110–1115. [[CrossRef](#)]
37. Hulbert, D.M.; Anders, A.; Dudina, D.V.; Anderson, J.; Jiang, D.; Unuvar, C.; Anselmi-Tamburini, U.; Lavernia, E.J.; Mukherjee, A.K. The absence of plasma in “spark plasma sintering”. *J. Appl. Phys.* **2008**, *104*, 033305. [[CrossRef](#)]
38. Srinivasarao, B.; Suryanarayana, C.; Oh-ishi, K.; Hano, K. Microstructure and Mechanical Properties of Al-Zr nanocomposite materials. *Mater. Sci. Eng. A* **2009**, *518*, 100–107. [[CrossRef](#)]
39. Liu, Z.F.; Zhang, Z.H.; Lu, J.F.; Korznikova, V.E.; Wang, F.C. Effect of sintering temperature on microstructures and mechanical properties of spark plasma sintered nanocrystalline aluminium. *Mater. Des.* **2014**, *64*, 625–630. [[CrossRef](#)]

40. Mondolfo, L.F. 4-Aluminum-Zinc Alloys. In *Aluminium Alloys: Structure and Properties*; Mondolfo, L.F., Ed.; Butterworth-Heinemann: London, UK, 1976; pp. 842–882. [[CrossRef](#)]
41. Hardy, H.K.; Heal, T.J. Report on precipitation. *Prog. Met. Phys.* **1954**, *5*, 143–278. [[CrossRef](#)]
42. Liu, J.Z.; Chen, J.H.; Yang, X.B.; Ren, S.; Wu, C.L.; Xub, H.Y.; Zoub, J. Revisiting the precipitation sequence in Al-Zn-Mg-based alloys by high-resolution transmission electron microscopy. *Scr. Mater.* **2010**, *63*, 1061–1064. [[CrossRef](#)]
43. El-Khalek, A.M.A. The variation of work-hardening characteristics of Al-1 wt % Si and Al-1 wt % Si-0.1 wt % Zr-0.1 wt % Ti alloys. *Phys. B Condens. Matter* **2002**, *315*, 7–12. [[CrossRef](#)]
44. Kim, I.H.; Kim, C.S.; Kim, K.T.; Kim, Z.H. Microstructural Characterization of Al-Zr Alloy with Nano-Sized Grains. *Key Eng. Mater.* **2006**, *326–328*, 429–432. [[CrossRef](#)]
45. Cahn, R.W. *Binary Alloy Phase Diagrams*, 2nd ed.; Massalski, T.B., Okamoto, H., Subramanian, P.R., Kacprzak, L., Eds.; ASM International: Materials Park, OH, USA, 1990. [[CrossRef](#)]
46. Lityńska-Dobrzyńska, L.; Ochin, P.; Góral, A.; Faryna, M.; Dutkiewicz, J. The Microstructure of Rapidly Solidified Al-Zn-Mg-Cu Alloys with Zr Addition. *Solid State Phenom.* **2010**, *163*, 42–45. [[CrossRef](#)]
47. Yazdian, N.; Karimzadeh, F.; Tavoosi, M. Microstructural evolution of nanostructure 7075 aluminum alloy during isothermal annealing. *J. Alloys Compd.* **2010**, *493*, 137–141. [[CrossRef](#)]
48. Patra, A.; Karak, S.K.; Pal, S. Effects of Mechanical Alloying on Solid Solubility. *Adv. Eng. Forum* **2016**, *15*, 17–24. [[CrossRef](#)]
49. Piela, K.; Blaž, L.; Sierpinski, Z.; Foryš, T. Non-isothermal annealing of AA7075 aluminum alloy-structural and mechanical effects. *Arch Metall. Mater.* **2012**, *57*, 703–709. [[CrossRef](#)]
50. Mondal, C.; Mukhopadhyay, A.K. On the nature of T(Al₂Mg₃Zn₃) and S(Al₂CuMg) phases present in as-cast and annealed 7055 aluminum alloy. *Mater. Sci. Eng. A* **2005**, *391*, 367–376. [[CrossRef](#)]
51. Das, S.K.; Davis, A. High-performance aerospace alloys via rapid solidification processing. *Mater. Sci. Eng.* **1988**, *98*, 1–12. [[CrossRef](#)]
52. Xie, G.; Ohashi, O.; Sato, T.; Yamaguchi, N.; Song, M.; Mitsuishi, K.; Furuya, K. Effect of Mg on the Sintering of Al-Mg Alloy Powders by Pulse Electric-Current Sintering Process. *Mater. Trans.* **2004**, *45*, 904–909. [[CrossRef](#)]



© 2017 by the authors. Licensee MDPI, Basel, Switzerland. This article is an open access article distributed under the terms and conditions of the Creative Commons Attribution (CC BY) license (<http://creativecommons.org/licenses/by/4.0/>).